PAPER

Check for updates

Lithiophilic nanoskin-enabled dendrite-free Li deposition in pomegranate-like carbon microclusters

Ho Rim Kim,†[a] Du Yeol Jo,†[b] Hong Geun Oh,[a] Jeong Ho Na,[a] Hyun Jin Kim,[a] Seong-Yong Jeong [ID] *[c] and Seung-Keun Park [ID] *[ab]

The pomegranate-like carbon microclusters (P-CMs), constructed from densely assembled hollow carbon spheres, provide interconnected internal voids that can accommodate Li and mitigate macroscopic volume changes. However, despite this advantageous architecture, Li deposition in P-CMs often remains surface-biased owing to insufficient interfacial lithiophilicity and non-uniform solid-electrolyte interphase formation. These interfacial limitations lead to localized Li nucleation, gradual Li accumulation on the outer surface, and eventual dendritic growth under prolonged cycling conditions. In this study, we applied a conformal polydopamine (PDA) nanoskin coating on the P-CM (the resulting sample is denoted as P-CM@PDA) to regulate its Li nucleation behavior and stabilize the interfacial chemistry. The PDA-derived catechol/amine functional groups provide abundant lithiophilic sites that lower the nucleation barrier and homogenize the Li^+ flux, while the hierarchical P-CM framework facilitates inward Li infusion through continuous ionic pathways. Consequently, P-CM@PDA achieves highly reversible Li plating/stripping, with a stable coulombic efficiency of ~97% for 150 cycles at 3.0 mA h cm^{-2}, and maintains long-term symmetric cell cycling for more than 450 h at 2.0 mA cm^{-2} and 1.0 mA h cm^{-2}. When paired with a $LiFePO_4$ cathode, the full cell delivers a high reversible discharge capacity of 141.8 mA h g^{-1} with >99% capacity retention over 350 cycles and superior rate capability up to 10C rate. This study demonstrates that interfacial lithiophilicity enhancement, rather than structural redesign alone, is the key to enabling dense, dendrite-free Li storage in hierarchical carbon hosts, providing a promising pathway to high-energy lithium metal batteries.

Introduction

Lithium metal has long been regarded as a leading candidate for next-generation anodes in lithium-ion batteries (LIBs) owing to its ultrahigh theoretical capacity (3860 mA h g^{-1}) and very low reduction potential (−3.04 V *vs.* standard hydrogen electrode).[1-6] Unlike conventional anodes, such as graphite and silicon, which undergo volume changes of approximately 10% and 400%, respectively, lithium metal exhibits theoretically unlimited relative volume fluctuations during cycling because metallic Li can deposit and strip without a host framework.[7-11] This host-free deposition not only amplifies volume instability but also aggravates dendritic growth, a phenomenon that is far more pronounced than that in traditional LIB systems.[12,13] Furthermore, Li-metal anodes suffer from severe interfacial instability in liquid electrolytes. Spontaneous reactions with the electrolyte generate a solid-electrolyte interphase (SEI) that initially passivates the surface but lacks mechanical robustness.[14-18] Repeated plating/stripping induces large volume changes and internal stress, fracturing the self-formed SEI, exposing fresh Li metal, and continuously consuming the electrolyte.[19-22] These effects are exacerbated by the uneven lithiophilicity of the substrate, non-uniform Li^+ flux, and local Li^+ depletion near active sites, resulting in dendritic growth, dead Li accumulation, low coulombic efficiency (CE), and safety concerns.[23-25] In essence, the battery fails due to the formation of a mechanically fragile, chemically heterogeneous SEI coupled with an uneven current/potential distribution driven by Li^+ concentration gradients.

Several strategies have been explored to stabilize Li-metal anodes, including electrolyte optimization and the use of functional additives that promote the *in situ* formation of more uniform SEI layers.[26-29] Although these electrolyte-driven approaches have improved the interphase chemistry of LIBs, the resulting SEI often remains insufficiently elastic to

[a]Department of Intelligent Energy and Industry, Chung-Ang University, 84 Heukseok-ro, Dongjak-gu, Seoul 06974, Republic of Korea. E-mail: skpark09@cau.ac.kr

[b]Department of Advanced Materials Engineering, Chung-Ang University, 4726, Seodong-daero, Daedeok-myeon, Anseong-si, Gyeonggi-do 17546, Republic of Korea

[c]Division of Advanced Materials Engineering, Kongju National University, Cheonan, 31080, Republic of Korea. E-mail: syjeong@kongju.ac.kr

† These authors contributed equally to this work.

17366 | *J. Mater. Chem. A*, 2026, 14, 17366–17374

This journal is © The Royal Society of Chemistry 2026

accommodate the continuous morphological evolution of the Li-metal anode, resulting in recurring fracture and repeated electrolyte decomposition.[30–33]

To address these limitations and restrain dendrite growth, carbon hosts with well-defined three-dimensional (3D) architectures have been proposed as effective physical scaffolds.[34–38] Their large surface areas and internal free volumes distribute the current, lower the local current density, and provide space to accommodate the deposited Li. Consequently, carbon materials with advantageous morphologies, such as those derived from carbon nanotubes, graphene frameworks, and metal–organic frameworks (MOFs), have been explored as Li hosts.[39–43] However, many of these hosts face scale-up barriers owing to complex fabrication routes, high costs, and the need for a substantial amount of binder to form electrodes. Even when available, particulate electrodes can exhibit high through-thickness tortuosity and a modest tap density, channeling Li^+ toward the top surface and causing "top-plating."

In our previous study, we demonstrated the feasibility of a spray drying-based hierarchical assembly strategy for constructing pomegranate-like carbon microclusters (P-CMs), in which primary hollow carbon spheres (HCSs) were densely packed while maintaining their internal voids.[44] This design preserves the intrinsic structural advantages of the individual HCSs while overcoming the limitations associated with nanoscale hosts, thereby enabling improved structural integrity, reduced binder demand, and lower electrode tortuosity. These features facilitate continuous and shortened electron/ion transport pathways, effectively mitigating top-surface Li plating and allowing Li to be stably accommodated within the internal voids of the primary spheres. Nevertheless, the P-CM host still relies on a spontaneously formed SEI, which remains chemically heterogeneous and mechanically vulnerable, especially at high current densities or large areal capacities. Such instability could cause localized Li^+ flux, uneven nucleation, and preferential Li plating near the top surface, resulting in excessive Li accumulation and dead Li formation. In this regard, the original P-CM architecture defined where Li could be stored, but did not actively regulate how or where Li nucleation and early-stage growth were initiated.

To overcome the limitations of the spontaneously formed SEI and to fundamentally alter the Li growth mode in the P-CM host, a conformal polymer nanolayer was introduced onto the P-CM surface. This artificial skin establishes a pre-defined interfacial chemistry that anchors Li^+ uniformly during nucleation, preventing stochastic deposition events that generally trigger dendrite formation.[45–47] At the molecular level, the polymer layer supplies lithiophilic coordination sites that lower the nucleation energy barrier and promote spatially homogeneous Li adsorption, while its viscoelastic and ion-permeable network buffers the interfacial strain and maintains uninterrupted Li^+ transport during cycling.[48,49] To satisfy these interfacial requirements, polydopamine (PDA) was selected as the functional coating material owing to its abundant catechol and amine ligands, strong adhesion, and intrinsic mechanical deformability.[44] The PDA forms a tightly conformal nanoskin around the P-CM scaffold *via in situ* oxidative self-

polymerization, creating a Li-affinitive and stress-adaptive interphase.[50–52] This pre-engineered hybrid framework synergistically couples the low-tortuosity 3D carbon host with dynamic interfacial regulation, enabling bottom-up Li filling within the internal voids, mitigating dead Li accumulation, and delivering dendrite-free deposition behavior with enhanced cycling stability and CE. Therefore, the Li metal could be effectively accommodated within the large internal voids of the HCS subunits in the P-CM framework, provided that inward Li infusion is promoted by interfacial regulation. This mechanism enabled stable Li deposition while minimizing surface-driven dendritic growth. Consequently, the P-CM@PDA host facilitated highly reversible Li cycling, sustaining a high CE of ~97% over 150 cycles at an areal capacity of 3 mA h cm^{-2}, and demonstrated long-term cycling stability over 450 h at 2 mA cm^{-2} and 1.0 mA h cm^{-2} in symmetric cells. Furthermore, when coupled with a $LiFePO_4$ (LFP) cathode, the full cell exhibited excellent capacity retention and stable cycling performance, confirming the practical applicability of the P-CM@PDA host for high-energy lithium-metal batteries.

Experiments

Synthesis of SiO_2@RF nanoparticles and P-CM

Silica-resorcinol-formaldehyde (SiO_2@RF) core–shell nanoparticles were synthesized following a previously reported procedure.[53] A homogeneous aqueous suspension of SiO_2@RF nanoparticles (15 g L^{-1}) was prepared with dextrin (5 g L^{-1}) as a processing aid. The suspension was spray-dried at a nozzle back-pressure of 2.0 bar and an outlet temperature of 100 °C to produce SiO_2@RF microclusters. The collected powder was carbonized at 700 °C for 3 h under Ar flow to convert the RF shell into carbon. The internal SiO_2 template was subsequently removed by etching in a 3.0 M NaOH solution, obtaining pomegranate-like carbon microclusters (P-CM).

Preparation of PDA-coated P-CM (P-CM@PDA)

To a apply the PDA coating, the P-CMs (0.15 g) were dispersed in 150 mL of Tris buffer (10 mM, pH 8.5) *via* bath sonication for 10 min. Dopamine·HCl (0.15 g) was then added (solid mass ratio of P-CM to dopamine = 1 : 1; total solid ≈ 1.0 g L^{-1}). The mixture was stirred at room temperature for 24 h in ambient air to induce the *in situ* oxidative self-polymerization of dopamine, forming a conformal PDA nanoskin on the carbon surface. The final product (P-CM@PDA) was collected *via* centrifugation, washed with deionized water, and dried under vacuum.
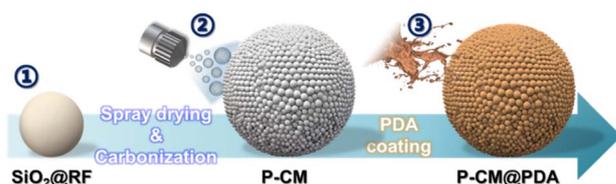

Fig. 1 Schematic illustration of the synthesis process of P-CM@PDA.

This journal is © The Royal Society of Chemistry 2026

J. Mater. Chem. A, 2026, **14**, 17366–17374 | **17367**

Results and discussion

As depicted in Fig. 1, monodisperse SiO_2 cores prepared by the Stöber method were coated with a RF shell to form SiO_2@RF nanoparticles (Fig. S1). A single-pass spray-drying step transformed the colloidal SiO_2@RF particles into dense spherical microclusters (a-SiO_2@C, Fig. S1c and d). The subsequent carbonization and alkaline etching processes led to P-CMs composed of tightly packed hollow subunits. Finally, conformal PDA nanoskin was introduced *via* the *in situ* oxidative self-polymerization of dopamine to obtain P-CM@PDA. This coating uniformly covered the carbon framework and preserved its hierarchical morphology, generating a continuous and mechanically compliant interface.

Fig. 2 shows the morphological and structural features of the P-CM@PDA host. The spray-drying process compacted numerous HCSs into well-defined spherical microclusters while retaining the internal voids of each subunit. As observed in the SEM image of the pristine HCS (Fig. S1a and b), the particles initially existed as isolated shells, but dextrin-assisted spray drying induced the assembly of a robust microsphere with a rough surface texture (Fig. S1c and d). The TEM analysis confirmed that the carbon shell was thin and continuous, and

that a hierarchical porous framework favorable for accommodating Li within the cluster interior was formed (Fig. 2b), consistent with the hollow architecture observed in pristine HCSs (Fig. S2).

After the PDA coating, the overall spherical geometry and corrugated surface characteristic of the P-CM were preserved (Fig. 2a and b), and a uniform conformal nanoskin (~13 nm) was clearly visible on the carbon shells (Fig. 2c). Energy-dispersive X-ray spectroscopy elemental mapping of carbon and nitrogen (Fig. 1d) further verified the homogeneous deposition of the N-containing PDA layer over the entire cluster surface, indicating complete interfacial coverage. Such conformal coverage ensures intimate interfacial contact and stable chemical coupling between the PDA skin and the underlying carbon framework.

The carbon skeleton of the P-CM host exhibited a broad (002) diffraction peak in the X-ray diffraction pattern (Fig. 2e) and characteristic D and G bands in the Raman spectrum (Fig. 2f), indicating an amorphous, defect-rich carbon framework. The X-ray Photoelectron Spectroscopy (XPS) analysis further confirmed the presence of C, O, and N species originating from the PDA layer (Fig. 2g). Spectral deconvolution of the N 1s region (Fig. 1h) resolved multiple components assigned to amine (R–NH_2), secondary amine (R–NH–R), and imine (R–N=R) functionalities, consistent with polymerized catecholamine structures.[54] These N/O-rich groups make the surface highly lithiophilic, reducing the Li nucleation overpotential and facilitating homogeneous Li deposition. Collectively, these characterizations confirmed that the hierarchical carbon architecture was well preserved after PDA modification and that a conformal, nitrogen-functionalized nanoskin was uniformly anchored on the microclusters, establishing a stable and chemically interactive interface.

To elucidate the effect of PDA surface modification on the Li nucleation pathway, the Li plating behavior was systematically
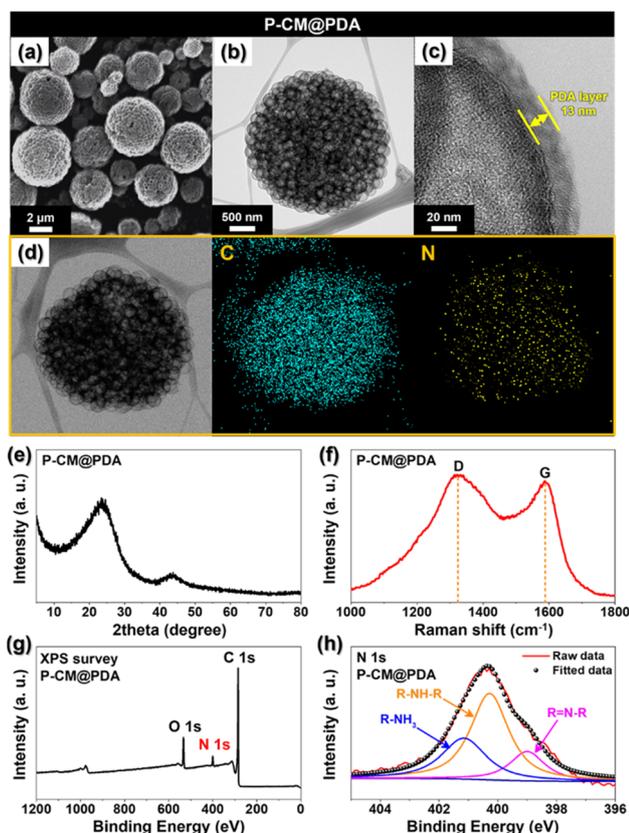

Fig. 2 Morphological, structural, and chemical characterization of P-CM@PDA. (a) SEM and (b and c) TEM images of P-CM@PDA, (d) EDS elemental mapping images for C and N in P-CM@PDA, (e) XRD pattern, (f) Raman spectrum, and (g) survey and (h) high-resolution N 1s XPS profiles of P-CM@PDA.
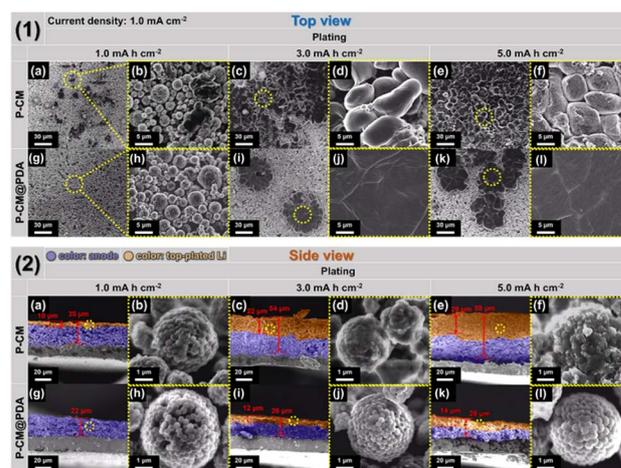

Fig. 3 Top- and cross-sectional SEM images of Li layers of increasing areal capacities plated on P-CM and P-CM@PDA hosts at 1 mA cm^{-2}. (1) Top-view SEM images after Li deposition of 1, 3, and 5 mA h cm^{-2} on P-CM (a–f) and P-CM@PDA (g–l) hosts. (2) Cross-sectional SEM images of P-CM (a–f), and P-CM@PDA (g–l).

17368 | *J. Mater. Chem. A*, 2026, **14**, 17366–17374

This journal is © The Royal Society of Chemistry 2026

investigated at 1 mA cm^{-2} and increasing areal capacities of 1, 3, and 5 mA h cm^{-2} (Fig. 3). At 1 mA h cm^{-2}, the P-CM electrode showed localized Li accumulation on the external surfaces of the microclusters, as evidenced by the irregular granular deposits in the top-view images (Fig. 3(1)a and b). The corresponding cross-sectional image (Fig. 3(2)a and b) reveals a top-plated Li layer of ~10 μm thickness loosely attached to the host scaffold and exhibiting visible interfacial gaps. In contrast, the P-CM@PDA electrode (Fig. 3(1)g and h) maintained a spherical cluster morphology with a smooth and uniform Li coating. The side-view profiles (Fig. 3(2)g and h) show a significantly thinner top-plated Li layer with strong interfacial contact, indicating that Li deposition is preferentially guided into the internal void network rather than accumulating on the external surface. Importantly, the key synergy does not arise from enhanced lithiophilicity alone, but from the coupling between nucleation regulation by the PDA nanoskin and spatially guided Li growth enabled by the hierarchical void architecture. When the plating capacity was increased to 3 mA h cm^{-2}, the morphological contrast became more pronounced. For P-CM, the top-view images (Fig. 3(1)c and d) display coalesced Li domains and partially fused surface clusters, accompanied by a thick, porous, and poorly adhered Li layer (~22 μm) in the cross-section (Fig. 3(2)c), confirming unstable Li growth driven by non-uniform current distribution. In contrast, P-CM@PDA (Fig. 3(1)i and j) preserved a compact and smooth surface without dendritic protrusions, while the cross-sectional Li layer remained dense and moderately thick (~12 μm) (Fig. 3(2)i), indicating that Li continued to fill the carbon scaffold, rather than building up externally. At the highest areal capacity of 5 mA h cm^{-2}, the P-CM electrode exhibited severe surface roughening and porous dendritic Li structures (Fig. 3(1)f), along with a thick and delaminated Li layer (~29 μm) (Fig. 3(2)e), demonstrating structural instability and uncontrolled Li overgrowth. In sharp contrast, P-CM@PDA (Fig. 3(1)k and l) maintained a dense and conformal Li coating with preserved microcluster morphology, and the side view of the sample (Fig. 3(2)k) shows a uniform, well-adhered Li layer (~14 μm), with no interfacial separation. This stable morphology indicates suppressed Li crowding, minimized SEI damage, and uniform ion flux throughout cycling. Collectively, these results confirm that while the uncoated P-CM primarily supports surface-dominated Li growth, causing rapid accumulation and dendritic expansion at high capacities, the P-CM@PDA electrode enables internalized, bottom-up Li filling promoted by the lithiophilic PDA coating. It should be noted that the morphological observations primarily demonstrate a suppressed surface accumulation behavior rather than a direct quantification of Li distribution within the internal voids. The synergy between the hierarchical microcluster voids and the uniform interfacial chemistry ensured compact, dendrite-free Li deposition with strong structural integrity.

Following the plating analysis, Fig. 4 presents the Li-stripping morphologies after depositing 3 mA h cm^{-2} of Li and delithiation to 80 mV at a current density of 1 mA cm^{-2}, providing direct insight into the reversibility of Li cycling. After being stripped, the uncoated P-CM electrode (Fig. 4(a and b))
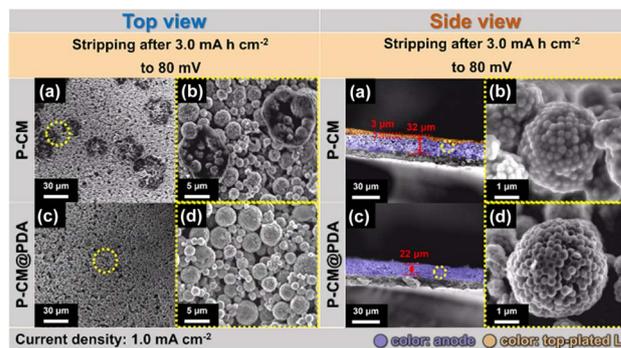

Fig. 4 Top- and cross-sectional SEM images of Li-stripping behavior after plating at 3 mA h cm^{-2} and 1 mA cm^{-2}, and delithiation to 80 mV. Top-view images of P-CM (a and b) and P-CM@PDA (c and d). Cross-sectional images of P-CM (a and b) and P-CM@PDA (c and d).

exhibited abundant residual porous Li and irregular voids scattered across the surface, as well as an uneven, discontinuous interface in the cross-section (Fig. 4(a and b)). The remaining Li layer, approximately 3 μm in thickness, indicated incomplete Li removal and the formation of "dead Li" regions that hindered uniform delithiation. This morphological degradation reflects poor interfacial stability and inefficient charge transfer during stripping, which is consistent with the inhomogeneous Li plating observed earlier. In contrast, the P-CM@PDA electrode (Fig. 4(c and d)) demonstrated a highly reversible Li-stripping behavior, with the spherical microcluster morphology almost completely restored and only a thin residual layer (~22 μm) of Li remaining, as shown in the side-view images (Fig. 4(c and d)). The surface was smooth and free of large pores, suggesting that Li was evenly extracted from both the outer and inner regions of the electrode. This reversibility confirmed that the conformal PDA coating effectively maintained an intimate interfacial contact during both plating and stripping, enabling uniform Li dissolution, without structural collapse. Consequently, the combined results shown in Fig. 3 and 4 demonstrate that the hierarchical P-CM framework and lithiophilic PDA nanoskin act synergistically to sustain compact, dendrite-free, and reversible Li cycling by mitigating interfacial detachment and facilitating homogeneous ion transport.

To further clarify the interfacial Li-ion transport and reaction kinetics of the hierarchical carbon hosts, linear polarization, Tafel analysis, and asymmetric cell tests were conducted on the HCS, P-CM, and P-CM@PDA electrodes (Fig. 5). Fig. 5a shows the linear polarization curves of the symmetric cells. The P-CM@PDA electrode exhibited the lowest overpotential slope, indicating the formation of an SEI layer with a smaller interfacial resistance and faster Li-ion diffusion than those of the P-CM and HCS electrodes. The PDA-derived functional groups (catechol and amine) served as lithiophilic sites that enhanced charge transfer and facilitated uniform Li nucleation. Using the corresponding Tafel plots (Fig. 5b), the exchange current densities (j_0) of HCS, P-CM, and P-CM@PDA were estimated to be 0.74, 0.89, and 0.99 mA cm^{-2}, respectively, confirming the

This journal is © The Royal Society of Chemistry 2026

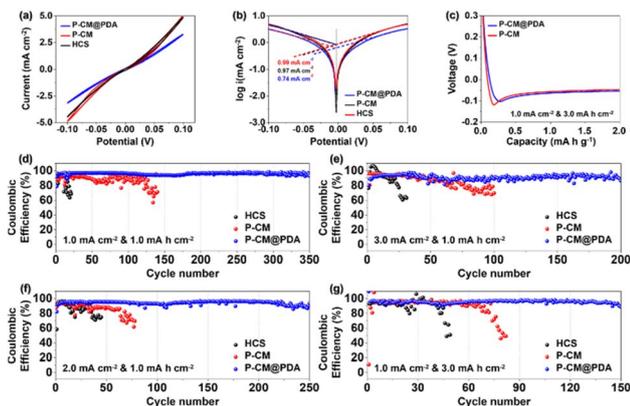*J. Mater. Chem. A*, 2026, **14**, 17366–17374 | **17369**

Fig. 5 (a) Linear polarization curves and (b) Tafel plots of symmetric cells using HCS and P-CM hosts as electrodes. (c) Voltage–capacity profiles obtained during initial Li plating at 1.0 mA cm^{-2} and 3.0 mA h cm^{-2} in asymmetric cells. (d–g) Coulombic efficiencies (CEs) of asymmetric cells under various cycling conditions: (d) 1.0 mA cm^{-2} and 1.0 mA h cm^{-2}, (e) 3.0 mA cm^{-2} and 1.0 mA h cm^{-2}, (f) 2.0 mA cm^{-2} and 1.0 mA h cm^{-2}, (g) 1.0 mA cm^{-2} and 3.0 mA h cm^{-2}.

superior interfacial kinetics of the PDA-modified electrode. In addition, cyclic voltammetry (CV) of the symmetric cells was conducted to further evaluate the interfacial reversibility during repeated plating/stripping (Fig. S4). Sequential CV scans (cycles 1–10) revealed distinct differences in the stabilization behavior among the three hosts. The HCS electrode showed gradually shifted and broadened CV curves, indicating continuous SEI reconstruction and sluggish interfacial charge transfer. In contrast, the P-CM electrode exhibited reduced hysteresis and faster curve convergence, reflecting improved Li$^+$ accessibility through the interconnected microcluster framework. Remarkably, P-CM@PDA displayed nearly overlapping CV profiles from the initial cycles, demonstrating rapid SEI stabilization and highly reversible Li nucleation/dissolution. This improvement originated from the strong chemical affinity between Li$^+$ and the N/O-rich PDA layer, which decreased the interfacial energy barrier for Li$^+$ desolvation and nucleation. In addition, the initial Li plating behavior was investigated in asymmetric cells at a current density of 1.0 mA cm^{-2} and areal capacity of 3.0 mA h cm^{-2} (Fig. 5c). The P-CM and P-CM@PDA electrodes exhibited similar initial overpotentials, with that of the P-CM@PDA electrode being only slightly lower. This result indicates that both hosts possess sufficient ion-transport pathways within their porous frameworks, enabling Li$^+$ migration into the electrode interior. However, the marginally smaller overpotential and smoother voltage response of P-CM@PDA suggest that the PDA layer further enhances interfacial wettability and charge transfer, leading to a more uniform Li$^+$ flux and homogeneous nucleation throughout the host structure. Therefore, the slightly reduced and more stable polarization of P-CM@PDA implies that Li preferentially deposits inside the interconnected voids, rather than accumulating on the external surface, contributing to compact and dendrite-free Li growth. The CE values of the asymmetric cells were evaluated at different current densities and areal capacities to assess the reversibility

and stability of Li plating/stripping on the three electrodes (HCS, P-CM, and P-CM@PDA). Under the moderate condition of 1.0 mA cm^{-2}/1.0 mA h cm^{-2} (Fig. 5d), the P-CM@PDA electrode exhibited a highly stable CE of ~99% throughout long-term cycling, with negligible fluctuations. In contrast, the P-CM electrode showed a gradual decline in CE from ~98% to ~95% after extended cycling, and the HCS electrode suffered pronounced CE decay within 20 cycles, accompanied by severe instability. These results demonstrate that the conformal PDA layer provides a chemically uniform Li-affinity surface and mechanically robust SEI, enabling durable Li reversibility, even under continuous cycling. When the current density was increased to 3.0 mA cm^{-2} while maintaining an areal capacity of 1.0 mA h cm^{-2} (Fig. 5e), the performance gap widened. The HCS electrode rapidly failed owing to dendritic growth and unstable interfacial contact, whereas the P-CM maintained moderate stability. In comparison, P-CM@PDA retained a nearly constant CE (>98%) over 200 cycles, highlighting its excellent tolerance to high-rate operation, which originated from the fast charge-transfer kinetics of the PDA-modified surface and the uniform Li$^+$ flux distribution within the 3D porous network. At 2.0 mA cm^{-2}/1.0 mA h cm^{-2} (Fig. 5f), the general trend persisted, with HCS exhibiting early failure, P-CM showing moderate durability, and P-CM@PDA consistently maintaining the highest CE (>98%) with minimal deviation. The superior reversibility of P-CM@PDA resulted from its dual regulation: structural voids that buffer Li volume changes and the lithiophilic PDA skin that ensures homogeneous Li nucleation and dissolution. Finally, when the areal capacity was increased to 3.0 mA h cm^{-2} at 1.0 mA cm^{-2} (Fig. 5g), the Li plating/stripping process became more demanding owing to the deposition of thicker Li layers and intensified SEI stress. Under these conditions, HCS exhibited rapid CE degradation and early short-circuiting, whereas P-CM exhibited a steady, yet noticeable drop in CE to a value below 95% after ~58 cycles. In contrast, P-CM@PDA continued to deliver a high and stable CE of ~98–99%, demonstrating its ability to sustain reversible Li cycling, even at high areal loading. Overall, the consistent CE superiority of P-CM@PDA across all current and capacity conditions underscores the synergistic benefits of the hierarchical carbon framework and the chemically active PDA coating. This combination provides efficient Li$^+$-transport pathways, ample voids for Li accommodation, and robust SEI integrity, thereby preventing dendrite growth and the accumulation of dead Li, even under aggressive cycling regimes.

To further investigate the chemical composition of the SEI layer and the role of the PDA layer, XPS analysis was conducted on the electrodes after 50 cycles. Fig. 6a and b show the C 1s spectra of P-CM@PDA and P-CM, respectively. Both electrodes exhibit typical SEI components, including C–C (284.8 eV), C–O (286.3 eV), and C=O (288.5 eV) peaks, which originate from the decomposition of the carbonate-based electrolyte.[55] The F 1s spectra provide more distinctive evidence of the PDA layer's influence. For both P-CM@PDA (Fig. 6c) and P-CM (Fig. 6d), the peaks corresponding to LiF (683.8 eV) and Li$_x$PO$_y$F$_z$ (685.3–685.7 eV) are observed.[56–58] Notably, the P-CM@PDA electrode exhibits a significantly higher relative intensity of the LiF peak

17370 | J. Mater. Chem. A, 2026, 14, 17366–17374

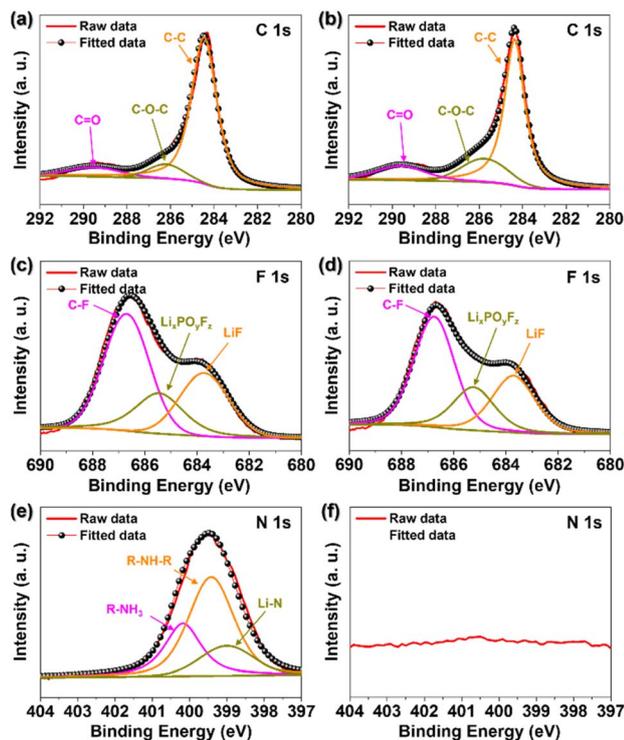This journal is © The Royal Society of Chemistry 2026

Fig. 6 Chemical composition of the SEI layers after 50 cycles. High-resolution XPS spectra of (a and b) C 1s, (c and d) F 1s, and (e and f) N 1s for (a, c and e) P-CM@PDA and (b, d and f) bare P-CM.
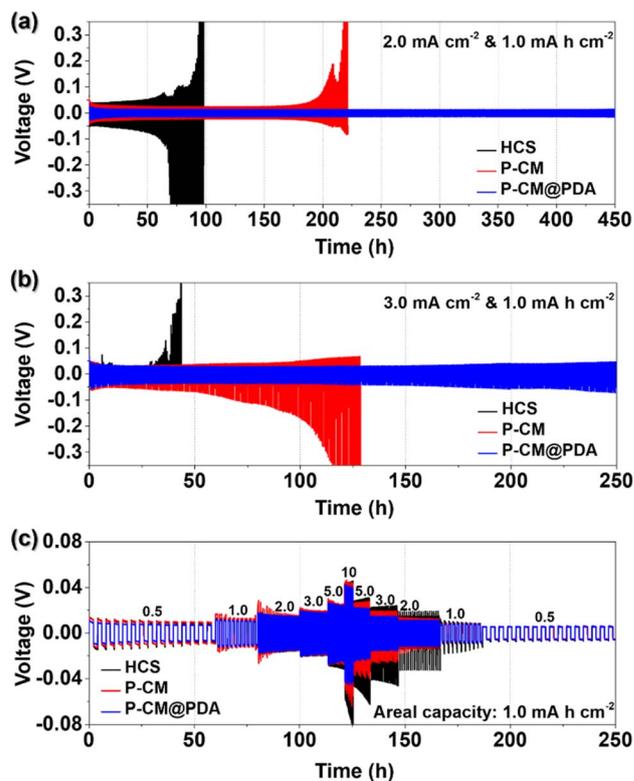

Fig. 7 Symmetric cycling stability evaluation of the P-CM and P-CM@PDA electrodes. (a and b) Voltage−time profiles recorded under continuous cycling at 2.0 and 3.0 mA cm^{-2} (1.0 mA h cm^{-2}). (c) Rate performance under stepwise current density variation from 0.5 to 10 mA cm^{-2}.

compared to the bare P-CM. This suggests that the PDA layer effectively regulates the electrolyte decomposition process, promoting the formation of a LiF-rich SEI, which is known to provide high ionic conductivity and mechanical stability. The most critical difference is observed in the N 1s spectra. While the bare P-CM electrode (Fig. 6f) shows no discernible nitrogen signal, the P-CM@PDA electrode (Fig. 6e) displays clear peaks at 399.3 eV and 400.2 eV, corresponding to amine/imine groups of PDA and Li–N species, respectively.[59] The emergence of the Li–N peak definitively proves that the nitrogen-containing functional groups of the PDA layer are chemically involved in the SEI formation, creating a lithiophilic environment that guides uniform Li deposition.

To further evaluate the cycling stability and interfacial reversibility of Li plating/stripping, symmetric cells were tested using the HCS, P-CM, and P-CM@PDA hosts under progressively increasing current conditions (Fig. 7). At 1.0 mA cm^{-2} (Fig. 7a), the HCS electrode exhibited a rapid rise in the overpotential and strong voltage fluctuations within the first 50 h, indicating unstable Li nucleation and repeated SEI rupture. In contrast, the P-CM electrode showed a more gradual evolution of the overpotential, reflecting improved Li accommodation within the internal voids of the microcluster framework. Notably, the P-CM@PDA electrode maintained the lowest and most stable polarization over extended cycling (~450 h), with minimal voltage noise, demonstrating highly reversible Li plating/stripping behavior. These results confirm that the PDA nanoskin promotes uniform Li$^+$ flux and accelerates SEI

stabilization, thereby preventing localized surface deposition. When the current density was increased to 3.0 mA cm^{-2} (Fig. 7b), the performance differences became more pronounced. The HCS-based cell experienced a sharp increase in the overpotential, followed by rapid cell failure owing to severe dendrite accumulation and interfacial delamination. The P-CM cell exhibited moderate stability but gradually developed increasing voltage hysteresis at 120 h, suggesting that Li began to migrate from the internal sites toward the external surface under high-rate conditions. In contrast, the P-CM@PDA cell maintained a stable and relatively low overpotential, even at a high current density, confirming that the PDA-mediated lithiophilic interface enabled uniform reaction kinetics and effectively suppressed high-current-induced dendritic propagation. To further probe the evolution of interfacial resistance during cycling, electrochemical impedance spectroscopy (EIS) was performed on P-CM//Li and P-CM@PDA//Li asymmetric-cells (Fig. S5). In the fresh state (Fig. S5a), the P-CM@PDA electrode exhibits a slightly larger semicircle, which can be attributed to the presence of the polymeric PDA nanoskin. However, after five plating/stripping cycles (Fig. S5b), the interfacial resistance of P-CM@PDA becomes noticeably smaller than that of bare P-CM. This reduction indicates the formation of a more stable and ionically conductive SEI, suggesting that the PDA layer facilitates interfacial stabilization

This journal is © The Royal Society of Chemistry 2026

J. Mater. Chem. A, 2026, 14, 17366–17374 | 17371

rather than impeding charge transfer during cycling. Under stepwise current density cycling (Fig. 7c), clear differences were observed in the interfacial robustness and reversibility of the three electrodes. At 1.0 mA cm^{-2}, the HCS electrode rapidly developed overpotential drift and irregular voltage oscillations, suggesting unstable SEI formation and surface-dominated Li accumulation. The P-CM electrode exhibited a relatively smoother voltage response, but showed a gradual increase in polarization when the current density increased to 3.0 mA cm^{-2}, indicating that Li deposition began to shift toward the external surface under higher ionic flux. In contrast, the P-CM@PDA electrode maintained a low and steady overpotential throughout the rate sequence, even after a transition to high-current operation and subsequent return to 1.0 mA cm^{-2}, demonstrating excellent interfacial elasticity and reversible Li-deposition behavior. This ability to recover and maintain stable polarization after high-rate stress confirms that the PDA nanoskin not only homogenizes the Li$^+$ flux but also mechanically stabilizes the SEI, preventing morphological memory effects and dendritic inheritance during cycling. Collectively, the rate performance of the symmetric cell indicates that while HCS undergoes unstable, surface-localized Li growth and P-CM partially buffers Li but struggles under a high current, P-CM@PDA enables structurally reversible, dendrite-free Li cycling across a broad range of operational current densities.

To demonstrate the practical applicability of the hierarchical carbon hosts in lithium-metal batteries, full cells were assembled by pairing a LiFePO$_4$ (LFP) cathode with each anode (HCS, P-CM, or P-CM@PDA) (Fig. 8). Recent studies on high-utilization lithium-metal batteries have primarily adopted strategies based on either excess Li metal foils or Li infusion into conductive frameworks to construct full cells.[60,61] In such approaches, metallic Li is typically introduced by melt

Fig. 8 Full-cell electrochemical performance of the P-CM@PDA and P-CM anodes paired with a LiFePO$_4$ (LFP) cathode. (a) Cycling performance at 1.0C over prolonged cycles. (b) Rate capability at various current densities from 0.2C to 10C.

infiltration, chemical infusion, or the use of thick Li foils, allowing sufficient Li reservoirs to sustain cycling while mitigating rapid capacity decay. These configurations have provided valuable insights into Li-metal degradation mechanisms and utilization limits under high areal capacities. However, the presence of excess Li inherently masks the intrinsic reversibility of the host structure and makes it difficult to decouple Li utilization efficiency from the buffering effect of an oversized Li reservoir. As a result, evaluating whether a host architecture can truly regulate Li deposition and dissolution under lean-Li conditions remains challenging in these systems. In contrast, the present work adopts a fundamentally different full-cell configuration based on electrochemically pre-plated Li, enabling a quantitatively controlled and limited Li inventory that directly reflects the reversibility of the host architecture rather than the availability of excess Li.

For full-cell assembly, the P-CM@PDA anode was pre-lithiated by electrochemical Li plating at 1.0 mA cm^{-2} to a fixed areal capacity of 5.0 mA h cm^{-2}, providing a limited and well-defined Li inventory. No thick Li foil was used in the full-cell configuration. The LFP cathode loading was 1.18 mg cm^{-2}, corresponding to an areal capacity of ~2.0–2.1 mA h cm^{-2}, while the P-CM@PDA anode loading was 1.12 mg cm^{-2}. Based on the pre-plated Li capacity, the resulting N/P ratio was approximately 2.3–2.5. At a cycling current of 1.0C, the HCS//LFP full cell exhibited rapid capacity deterioration and eventual short-circuit failure after ~130 cycles, which is attributed to unstable Li plating on the HCS electrode and the progressive accumulation of electrically isolated dead Li (Fig. 8a). In contrast, the P-CM//LFP cell exhibited improved cycling stability and maintained a reversible capacity over 300 cycles. However, the gradual capacity decay and reduced CE indicate the incomplete suppression of interfacial degradation and Li deposition instability. Strikingly, the P-CM@PDA//LFP cell exhibited the most robust cycling reversibility, retaining a high discharge capacity of 141.8 mA h g^{-1} and >99% CE after 300 cycles. The stable voltage plateau and minimal hysteresis during cycling confirmed the structurally reversible Li deposition/dissolution and strong interfacial integrity between the pre-lithiated scaffold and the electrolyte. The evolution of the charge–discharge profiles during cycling further highlights the different interfacial behaviors (Fig. S6a–c). The HCS//LFP full cell exhibited significant broadening and distortion of the voltage profiles after ~330 cycles, indicating a severe loss of active Li and increasing polarization. The P-CM//LFP cell exhibited moderate profile distortion, implying the partial stabilization of Li cycling. In contrast, the P-CM@PDA//LFP cell maintained nearly overlapping GCD curves over extended cycling, confirming that the PDA-modified hierarchical carbon framework effectively accommodates Li without inducing an irreversible Li buildup or structural degradation. Electrochemical impedance spectroscopy measurements performed after 55 cycles (Fig. S6d) supported these observations. The charge-transfer resistance (R_{ct}) followed the order of P-CM@PDA < P-CM < HCS, with P-CM@PDA exhibiting the smallest semicircle diameter. This reduction in the interfacial resistance arises from the lithiophilic PDA nanoskin, which
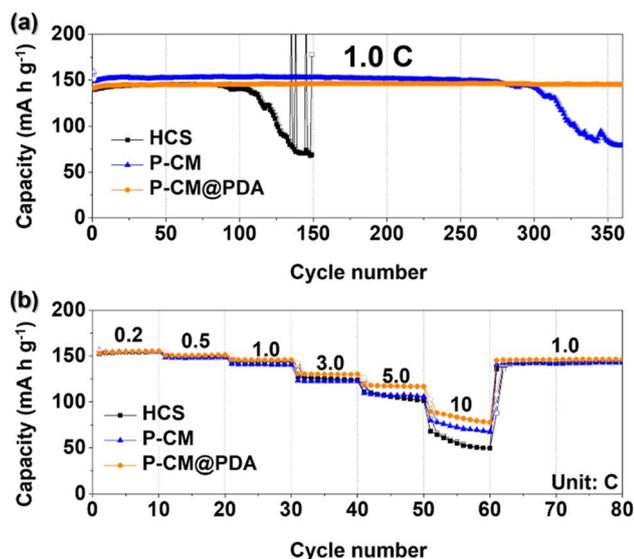
17372 | J. Mater. Chem. A, 2026, 14, 17366–17374

This journal is © The Royal Society of Chemistry 2026

introduces abundant polar functional groups (catechol and amine), improving wetting and enabling uniform Li^+ flux during cycling. The superior interfacial stability of the P-CM@PDA anode is further reflected in its rate performance (Fig. 8b). While both HCS//LFP and P-CM//LFP maintain reasonable capacities at moderate current densities ($\leq$5.0C), the HCS//LFP cell undergoes abrupt capacity decay at a higher current (10.0C), consistent with its unstable interfacial Li handling. In contrast, the P-CM//LFP cell showed improved retention, yet still suffered from polarization-induced capacity loss. Conversely, the P-CM@PDA//LFP cell maintained a high reversible capacity, even at 10.0C, demonstrating accelerated charge-transfer kinetics and suppressed Li dendrite formation under high-rate cycling. Collectively, these full-cell evaluations confirm that the hierarchical P-CM scaffold provides internal Li-storage sites, and that the PDA-derived lithiophilic surface layer ensures uniform nucleation, dense Li packing, and reversible Li transport, enabling the long-term, high-rate, and stable operation of the Li-metal full cell.

Conclusions

This study demonstrates that uniformly assembling hollow carbon spheres into dense pomegranate-like microclusters enables efficient Li accommodation within the internal voids, while conformal PDA nanoskin serves as a lithiophilic and mechanically adaptive interphase. The hierarchical P-CM framework reduced electrode tortuosity and facilitated preferential inward Li accommodation, while the PDA layer regulated Li nucleation behavior and contributed to SEI stabilization. Collectively, these structural and chemical contributions effectively suppressed dendritic growth and mitigated dead Li accumulation. Consequently, the P-CM@PDA host achieved highly stable Li reversibility, maintaining ~97% coulombic efficiency at 3.0 mA h cm^{-2} and sustaining long-term cycling (>450 h) at 2.0 mA cm^{-2} in symmetric cells. When implemented in full cells with a $LiFePO_4$ cathode, the P-CM@PDA anode exhibited high-capacity retention (141.8 mA h g^{-1}), >99% CE after 350 cycles, and outstanding rate performance up to 10C, outperforming both unmodified P-CM and HCS hosts. These results suggest that interfacial chemistry engineering, when coupled with hierarchical void-confined Li storage, provides a robust pathway to dendrite-free and long-lived Li metal anodes. The strategy described herein is synthetically scalable, compositionally versatile, broadly compatible, and offers a practical route to next-generation high-energy lithium metal batteries.

Author contributions

Ho Rim Kim: writing – original draft, visualization, methodology, investigation, formal analysis, data curation, conceptualization. Do Yeol Jo: writing – original draft, visualization, methodology, investigation, formal analysis. Hong Geun Oh: writing – review & editing, visualization, methodology, investigation, formal analysis. Hyun Jin Kim: writing – review & editing, visualization, methodology, investigation, formal analysis. Seong-Yong Jeong: writing – review & editing, software, resources, investigation, visualization. Seung-Keun Park: writing – review & editing, supervision, software, resources, project administration, funding acquisition, conceptualization.

Conflicts of interest

There are no conflicts to declare.

Data availability

Acknowledgements

Notes and references

1 D. Lin, Y. Liu and Y. Cui, *Nat. Nanotechnol.*, 2017, **12**, 194–206.

2 K.-S. Chen, I. Balla, N. S. Luu and M. C. Hersam, *ACS Energy Lett.*, 2017, **2**, 2026–2034.

3 J. B. Goodenough and Y. Kim, *Chem. Mater.*, 2010, **22**, 587–603.

4 K.-H. Chen, K. N. Wood, E. Kazyak, W. S. LePage, A. L. Davis, A. J. Sanchez and N. P. Dasgupta, *J. Mater. Chem. A*, 2017, **5**, 11671–11681.

5 J. Cao, D. Zhang, X. Zhang, M. Sawangphruk, J. Qin and R. Liu, *J. Mater. Chem. A*, 2020, **8**, 9331–9344.

6 S. Cui, P. Zhai, W. Yang, Y. Wei, J. Xiao, L. Deng and Y. Gong, *Small*, 2020, **16**, 1905620.

7 Z. A. Ghazi, Z. Sun, C. Sun, F. Qi, B. An, F. Li and H. Cheng, *Small*, 2019, **15**, 1900687.

8 J.-M. Tarascon and M. Armand, *nature*, 2001, **414**, 359–367.

9 M. Obrovac and L. Christensen, *Electrochem. Solid State Lett.*, 2004, **7**, A93.

10 X.-B. Cheng, R. Zhang, C.-Z. Zhao and Q. Zhang, *Chem. Rev.*, 2017, **117**, 10403–10473.

11 H. Wang, Y. Liu, Y. Li and Y. Cui, *Electrochem. Energy Rev.*, 2019, **2**, 509–517.

This journal is © The Royal Society of Chemistry 2026

J. Mater. Chem. A, 2026, **14**, 17366–17374 | **17373**

12 X.-B. Cheng, R. Zhang, C.-Z. Zhao and Q. Zhang, *Chem. Rev.*, 2017, **117**, 10403–10473.

13 M. D. Tikekar, S. Choudhury, Z. Tu and L. A. Archer, *Nat. Energy*, 2016, **1**, 1–7.

14 E. Peled and S. Menkin, *J. Electrochem. Soc.*, 2017, **164**, A1703.

15 X.-B. Cheng, R. Zhang, C.-Z. Zhao and Q. Zhang, *Chem. Rev.*, 2017, **117**, 10403–10473.

16 K. Xu, *Chem. Rev.*, 2014, **114**, 11503–11618.

17 X. Yi, H. Fu, A. M. Rao, Y. Zhang, J. Zhou, C. Wang and B. Lu, *Nat Sustainability*, 2024, **7**, 326–337.

18 L. Habib, G. Suo, C. Lin, J. Li, S. Javed, K. Naseem and Z. K. Kalkozova, *Renewable Sustainable Energy Rev.*, 2025, **217**, 115721.

19 T. Liu, L. Lin, X. Bi, L. Tian, K. Yang, J. Liu, M. Li, Z. Chen, J. Lu and K. Amine, *Nat. Nanotechnol.*, 2019, **14**, 50–56.

20 C. Monroe and J. Newman, *J. Electrochem. Soc.*, 2005, **152**, A396.

21 J. Liu, H. Yuan, H. Liu, C. Zhao, Y. Lu, X. Cheng, J. Huang and Q. Zhang, *Adv. Energy Mater.*, 2022, **12**, 2100748.

22 K. N. Wood, M. Noked and N. P. Dasgupta, *ACS Energy Lett.*, 2017, **2**, 664–672.

23 K. Yan, Z. Lu, H.-W. Lee, F. Xiong, P.-C. Hsu, Y. Li, J. Zhao, S. Chu and Y. Cui, *Nat. Energy*, 2016, **1**, 1–8.

24 Y. Cheng, X. Ke, Y. Chen, X. Huang, Z. Shi and Z. Guo, *Nano Energy*, 2019, **63**, 103854.

25 Y. Xu, K. Dong, Y. Jie, P. Adelhelm, Y. Chen, L. Xu, P. Yu, J. Kim, Z. Kochovski and Z. Yu, *Adv. Energy Mater.*, 2022, **12**, 2200398.

26 Y. Zhang, Z. Yuan, B. Xie, J. Cao, H. Zhang, S. Zhang, D. Wang, F. Sun, X. Du and J. Zhang, *Adv. Funct. Mater.*, 2025, 2504367.

27 K. Schroder, J. Alvarado, T. A. Yersak, J. Li, N. Dudney, L. J. Webb, Y. S. Meng and K. J. Stevenson, *Chem. Mater.*, 2015, **27**, 5531–5542.

28 Q. Zhang, A. Yang, M. Wang and W. Gao, *Chem. Eng. J.*, 2025, 163756.

29 J. Wang, Q. Zheng, M. Fang, S. Ko, Y. Yamada and A. Yamada, *Adv. Sci.*, 2021, **8**, 2101646.

30 Y. Zhang, Y. Zhong, S. Liang, B. Wang, X. Chen and H. Wang, *ACS Mater. Lett.*, 2019, **1**, 254–259.

31 X. Shen, R. Zhang, X. Chen, X. Cheng, X. Li and Q. Zhang, *Adv. Energy Mater.*, 2020, **10**, 1903645.

32 I. Yoon, S. Jurng, D. P. Abraham, B. L. Lucht and P. R. Guduru, *Energy Storage Mater.*, 2020, **25**, 296–304.

33 K. N. Wood, M. Noked and N. P. Dasgupta, *ACS Energy Lett.*, 2017, **2**, 664–672.

34 W. Wu, D. Ning, J. Zhang, G. Liu, L. Zeng, H. Yao, M. Wang, L. Deng and L. Yao, *Energy Storage Mater.*, 2023, **63**, 102974.

35 Y. Zhou, D. Yan, D. Kalyon and J. C. Kim, *ACS Appl. Energy Mater.*, 2024, **7**, 7176–7184.

36 C. Yang, H. Yue, H. Yao, F. Niu, M. Wang, B. Chen, Z. Lu, D. Ning, C. Yang and W. Wu, *J. Alloys Compd.*, 2024, **1008**, 176799.

37 M. Zhou, S.-X. Yan, Q. Wang, M.-X. Tan, D.-Y. Wang, Z.-Q. Yu, S.-H. Luo, Y.-H. Zhang and X. Liu, *Rare Met.*, 2022, **41**, 2280–2291.

38 C. Lin, G. Suo, R. Mu, B. Zhao, J. Li, X. Hou, X. Ye, Y. Yang and L. Zhang, *J. Power Sources*, 2024, **623**, 235426.

39 Y. Liu, D. Lin, P. Y. Yuen, K. Liu, J. Xie, R. H. Dauskardt and Y. Cui, *Adv. Mater.*, 2017, **29**, 1605531.

40 X. Nie, A. Zhang, Y. Liu, C. Shen, M. Chen, C. Xu, Q. Liu, J. Cai, A. Alfaraidi and C. Zhou, *Energy Storage Mater.*, 2019, **17**, 341–348.

41 M. Song, Y. Li, L. Gao, R. Zhao, Y. Xu, S. Han, J. Zhu, L. Wang and Y. Zhao, *Small*, 2024, **20**, 2306187.

42 L. Wang, X. Zhu, Y. Guan, J. Zhang, F. Ai, W. Zhang, Y. Xiang, S. Vijayan, G. Li and Y. Huang, *Energy Storage Mater.*, 2018, **11**, 191–196.

43 B. Zhao, G. Suo, R. Mu, C. Lin, J. Li, X. Hou, X. Ye, Y. Yang and L. Zhang, *J. Colloid Interface Sci.*, 2025, **677**, 637–646.

44 D. Y. Jo, J. B. Lim, J. K. Kim, Y. C. Kang and S.-K. Park, *Rare Met.*, 2025, **44**, 95–109.

45 N. Li, Y. Yin, C. Yang and Y. Guo, *Adv. Mater.*, 2016, **28**, 1853–1858.

46 J. Sun, S. Zhang, J. Li, B. Xie, J. Ma, S. Dong and G. Cui, *Adv. Mater.*, 2023, **35**, 2209404.

47 D. Kang, M. Xiao and J. P. Lemmon, *Batter. Supercaps*, 2021, **4**, 445–455.

48 E. Cha, J. H. Yun, R. Ponraj and D. K. Kim, *Mater. Chem. Front.*, 2021, **5**, 6294–6314.

49 N. Li, Q. Ye, K. Zhang, H. Yan, C. Shen, B. Wei and K. Xie, *Angew. Chem.*, 2019, **131**, 18414–18419.

50 M. Saraf, Prateek, R. Ranjan, B. Balasubramaniam, V. K. Thakur and R. K. Gupta, *Adv. Mater. Interfaces*, 2024, **11**, 2300670.

51 W. Jiang, X. Yang, J. Deng, J. Zhang and G. Zhang, *J. Mater. Sci.*, 2021, **56**, 19359–19382.

52 J. Qin, J. Shi, K. Huang, P. Lu, P. Wen, F. Xing, B. Yang, M. Ye, Y. Yu and Z.-S. Wu, *Nat. Commun.*, 2021, **12**, 5786.

53 J.-S. Park, S. Y. Yang, J.-K. Lee and Y. C. Kang, *J. Mater. Chem. A*, 2022, **10**, 17790–17800.

54 H. Hemmatpour, O. De Luca, D. Crestani, M. C. Stuart, A. Lasorsa, P. C. van der Wel, K. Loos, T. Giousis, V. Haddadi-Asl and P. Rudolf, *Nat. Commun.*, 2023, **14**, 664.

55 Z. Hou, P.-F. Wang, X. Sun, W. Li, C. Sheng and P. He, *J. Electron. Mater.*, 2022, **51**, 4772–4779.

56 T. D. Pham, A. B. Faheem, H. D. Nguyen, H. M. Oh and K.-K. Lee, *J. Mater. Chem. A*, 2022, **10**, 12035–12046.

57 Y. Gu, L. Yang, S. Luo, E. Zhao and N. Saito, *Ionics*, 2022, **28**, 3743–3759.

58 Y. Li, Y. An, Y. Tian, H. Fei, S. Xiong, Y. Qian and J. Feng, *J. Electrochem. Soc.*, 2019, **166**, A2736–A2740.

59 X. Sun, S. Yang, T. Zhang, Y. Shi, L. Dong, G. Ai, D. Li and W. Mao, *Nanoscale*, 2022, **14**, 5033–5043.

60 P. Du, C. Yuan, X. Cui, K. Zhang, Y. Yu, X. Ren, X. Zhan and S. Gao, *J. Mater. Chem. A*, 2022, **10**, 8424–8431.

61 S. Jiao, J. Zheng, Q. Li, X. Li, M. H. Engelhard, R. Cao, J.-G. Zhang and W. Xu, *Joule*, 2018, **2**, 110–124.

17374 | *J. Mater. Chem. A*, 2026, **14**, 17366–17374

This journal is © The Royal Society of Chemistry 2026